Chemical Engineering Journal 511 (2025) 161931

Contents lists available at ScienceDirect

Chemical Engineering Journal

journal homepage: www.elsevier.com/locate/cej

Pore microstructure and mass transfer dynamics in thick electrodes for high energy density lithium-ion batteries

Bowei Li [a,b], Shanfeng Wang [d], Pan He [c,*], Zhenyao Huang [a], Bo Mai [a], Xia Zhang [f], Yuhang Chen [a], Yuehua Wen [a], Xiaqing Ran [a], Chunhua Han [a], Ingo Manke [f], Kang Dong [b,*], Mengyu Yan [a,e,*]

[a] State Key Laboratory of Silicate Materials for Architectures, International School of Materials Science and Engineering, Wuhan University of Technology, Wuhan 430070, PR China
[b] Multi-disciplinary Research Division, Institute of High Energy Physics Chinese Academy of Sciences, Beijing 100049, PR China
[c] Department of Chemistry, University College London, London WC1H 0AJ, UK
[d] Beijing Synchrotron Radiation Facility, X-ray Optics and Technology Laboratory, PR China
[e] Zhongyu Feima New Material Technology Innovation Center (Zhengzhou) Co., Ltd., High Technology Industrial Development Zone, No. 60 Xuelan Road, Zhengzhou 450001, PR China
[f] Institute of Electrochemical Energy Storage, Helmholtz-Zentrum Berlin für Materialien und Energie, Berlin 14109, Germany

ARTICLE INFO

Keywords:
Porosity
Tortuosity
Ion transport
Thick electrode
Pore distribution

ABSTRACT

Developing high-mass-loading electrodes holds great promise for enhancing the energy density of Li-ion batteries. However, increasing mass loading also leads to thicker electrodes, significantly altering the electrode's microstructure. Using advanced multi-scale imaging, the three-dimensional pore structure and mass transfer dynamic at micro-meter scale in both thick and thin $LiCoO_2$ and their impacts on electrochemical performance and redox homogeneity at nano-scale are investigated. We demonstrate that the halved porosity and increased tortuosity in thick electrodes result in poor electrolyte infiltration, which is a key factor contributing to capacity degradation. This finding underscores the critical role of wetting in thick electrodes and necessitates the need to optimize pore distribution, porosity, and tortuosity when thick electrodes are employed to boost the energy density of Li-ion batteries.

1. Introduction

With the advent of long-range electric vehicles, the requirement for driving range per charge has increased to 500 km [1]. However, modern mainstream electric vehicles powered by lithium-ion batteries (LIBs) typically achieve 200–300 km per charge, largely constrained by the limited energy density of commercial LIBs (approximately 250 Wh/kg and 770 Wh/L) [2–4]. Significant efforts have been put into improving the energy density of LIBs [5,6]. One of the strategies is exploring high-energy–density battery systems such as Mn-rich ($Li_{1.5}Ni_{0.25}Mn_{1.25}O_{3.5}$) cathode whose mass-energy density is up to 1100 Wh/kg [7]. Besides, optimizing the electrode structure can increase the battery mass loading (almost 100 mg/cm^2) and have a long life span [8]. Lastly, using battery packing techniques (i.e., blade batteries) to increase the energy density is a practical and effective strategy [9]. Among them, increasing the mass loading of the electrode to enhance the ratio of active material mass to inactive mass holds significant promise for boosting the energy density of the system. This approach is particularly advantageous as it aligns seamlessly with electrode manufacturing processes. For example, with the mass loading of commercial electrode $LiNi_{0.6}Mn_{0.2}Co_{0.2}O_2$ increasing from 6 mg/cm^2 to 20 mg/cm^2, the corresponding battery mass-energy density can be enhanced by roughly 40 % [10]. Whereas, the increase in mass loading can also lead to an increase in electrode thickness, which causes a series of undesirable effects, including the complexity of the coating process [11,12], the difficulty in the regulation of pore structure/tap density [13], and the increase in tortuosity [14,15]. As a result, the capacity fades rapidly in such a high-thick electrode battery system.

Significant progress has been achieved in understanding the battery performance deterioration of thick electrodes [16]. For example, several

* Corresponding authors at: State Key Laboratory of Silicate Materials for Architectures, International School of Materials Science and Engineering, Wuhan University of Technology, Wuhan 430070, PR China..
E-mail addresses: pan.he@ucl.ac.uk (P. He), dongkang@ihep.ac.cn (K. Dong), ymy@whut.edu.cn (M. Yan).

https://doi.org/10.1016/j.cej.2025.161931
Received 30 December 2024; Received in revised form 25 February 2025; Accepted 23 March 2025
Available online 27 March 2025

theoretical models have been developed to simulate the effect of porosity on the ion transport in thick electrodes [17]. These studies reveal that the capacity of thick electrodes declines rapidly at high current rates and that cathode thickness has a pronounced impact on specific energy. Appiah et al. utilized mathematical modeling to simulate the impact of varying electrode thickness and porosity on Li-ions transport [18]. Boyce et al. demonstrated through image-based modeling that increasing the porosity at the interface between the cathode and the separator can significantly enhance high-rate performance.[19] Fu et al. argue that compared to thin electrodes, thick electrodes are more sensitive to parameters such as porosity. Furthermore, they assert that strong dynamic constraints make thermodynamic failure the primary cause of capacity loss [20]. However, simulation methods have notable limitations [21,22]. Most simulation approaches rely on averaged values rather than calculating porosity variations across different electrode depths [23]. Additionally, conventional Butler–Vermer models fail to account for the concentration-dependent Li insertion/withdrawal process at the solid side of the electrode/electrolyte interface, leading to discrepancies in the calculated current density and overpotential [24]. Furthermore, studies have shown that thick electrodes with low porosity significantly reduce a battery's capacity retention rate, which declines sharply as current density increases [25]. However, the complexity of pore distribution, along with thickness and tortuosity, makes these properties challenging to characterize, as traditional techniques are unable to probe such thick electrodes [26,27]. Consequently, most investigations into their failure mechanisms are limited to theoretical simulations, leaving the precise causes of rapid capacity fading largely unresolved. Therefore, advanced characterization techniques is crucial and urgent for gaining a deeper understanding of the mass transfer mechanisms in thick electrodes.

Herein, we utilize synchrotron radiation micro-CT imaging (micro-CT) and transmission X-ray microscopy with X-ray absorption near-edge structure (TXM-XANES) to investigate the relationship between the structure and performance of thick electrodes [28–30]. These methods provide more intuitive and accurate insights compared to conventional simulations [31–34]. Our findings reveal that limited electrolyte infiltration dynamics is a critical factor contributing to capacity degradation, primarily driven by the non-uniform pore distribution, low porosity, and high tortuosity in thick electrodes.

2. Results and discussions

$LiCoO_2$ (LCO) electrodes were made by blading coating followed by a calendaring process to achieve a desired tap density (see *methods*). The mass loading of the low-mass loading electrode (LMLE) and high-mass loading electrode (HMLE) is ~ 20 mg/cm^2 and ~ 50 mg/cm^2, respectively, corresponding to a thickness of ~ 68 μ m and ~ 190 μ m (Fig. 1a-b and Fig. S1). Note that as a model material, commercial $LiCoO_2$ particles were employed with particle size around 12 μm (Fig. 1c). The micrometer structures of both electrodes were further imaged by synchrotron X-ray tomography (sample test method is shown in Fig. S2). As shown in Fig. 1d, three-dimensional (3D) tomograms reveals that LMLE contains relatively large pores, forming a pore network with lower curvature. In contrast, HMLE exhibits smaller pores and a more intricate pore structure, indicating more complex and extended Li-ion transport paths. However, when considering electrode thickness, the relative number of transport paths in HMLE is lower..The pore structure distributions in LMLE and HMLEs were quantitatively analyzed along the thickness direction of the electrode (Fig. 1e). The pore distribution of the LMLE from separator to current collector appears to be relatively uniform. Conversely, the HMLE displays an uneven pore structure with smaller unevenness on both sides facing separator/collector and a uniformly graded pore structure in the middle. Overall, the LMLE exhibits a higher porosity of 0.213, compared with a porosity of 0.115 for HMLE.

Furthermore, the tortuosity of LMLE and HMLEs was calculated according to the pore distribution from micro-CT results (see *Note 1 in SI*). As shown in Fig. 2a, the tortuosity of the HMLE is 1.77, which is 33 % higher than that of the LMLE (1.33), indicating a detour of mass transfer in the HMLE. To compare the mass transfer properties in these two electrodes, the MacMullin Number (N_m) was calculated via the empirical ratio (τ/ε) between tortuosity (τ) and porosity (ε), where higher values indicate greater resistance of mass transport.[11,35] The N_m of electrodes was obtained both from EIS testing and micro-CT. As shown in Fig. 2b, the impedance plots of symmetric batteries from HMLEs display a resistance of 42.42 Ω, which is 36.21 Ω higher than that of LMLEs (Table S3). The corresponding N_m of the HMLE is 15.53, which is 2.4 times that of LMLEs, indicating that the diffusion of Li ions in HMLE is more difficult (Fig. 2c, see *Note 2 in SI*). Notably, similar results were obtained from the micro-CT characterizations, which further validate the N_m differences between these two electrodes based on their

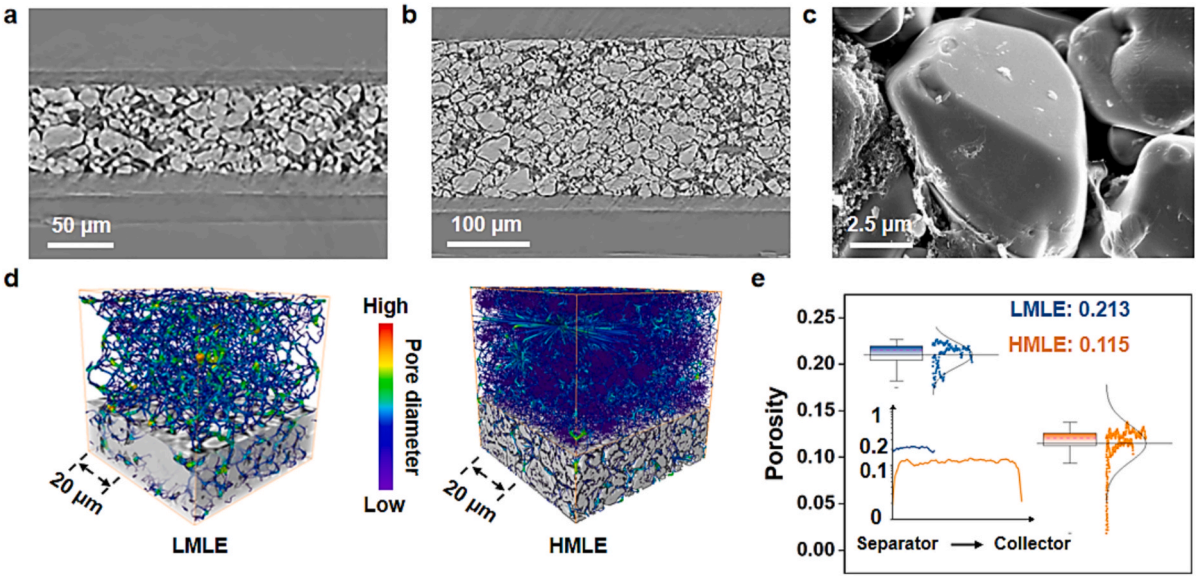

Fig. 1. The micro-meter structure characterization of $LiCoO_2$ electrode. The cross-sectional micro-CT images of (a) LMLE and (b) HMLE. (c) The SEM image of $LiCoO_2$ with a particle size ~ 12 μm. (d) 3D CT reconstruction images show the skeletal and porous structures of LMLE and HMLE; Gray for the electrode skeleton and the rest for pore distribution. (e) A box plot shows the porosity of LMLE and HMLE, and the inset shows typical pore distribution curves along the thickness direction.

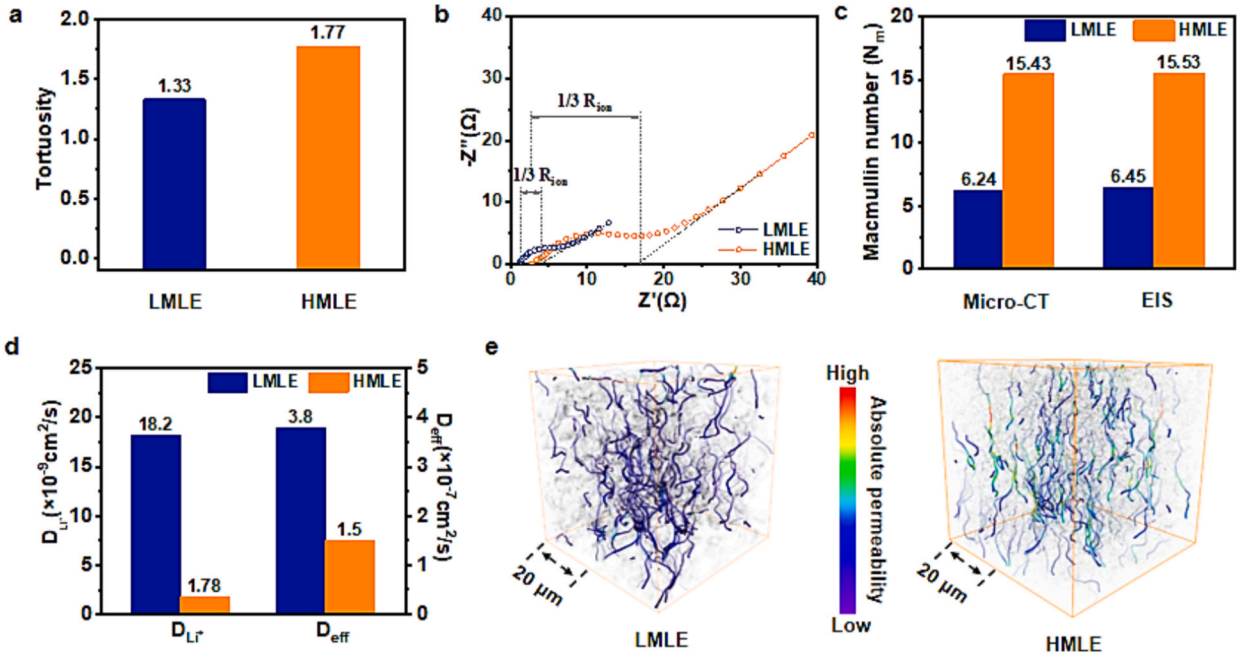

Fig. 2. Li-ion transport and electrolyte migration in LMLE and HMLE. (a) The tortuosity comparison of LMLE and HMLE (b) The EIS plots of the LMLE and HMLE from LCO symmetrical cells. (c) The MacMullin numbers of LMLE and HMLEs as calculated both from micro-CT and EIS. (d) The comparison of average solid-phase intrinsic diffusion coefficient (D_{Li+}) and electrolyte penetration coefficient (D_{eff}) of LMLE and HMLEs. (f) The 3D streamlined images show the electrolyte penetration in LMLE and HMLE's skeletons (grey color), with dynamic penetration processes shown in video 1.

structural properties. To investigate ion transport behavior in $LiCoO_2$ particles of different thicknesses electrodes, the galvanostatic intermittent titration technique (GITT) was employed. During both charging and discharging, the LMLE exhibited an average solid-phase intrinsic diffusion coefficient (D_{Li}^{+}) of 1.82×10^{-8} cm^2/s, which is 10 times that in HMLE (Fig. 2d and Fig. S3). Furthermore, the effective electrolyte diffusion (D_{eff}) was calculated with the Nernst-Einstein equation based on the parameters of porosity and tortuosity (see *Note 3 in SI*), which is approximately equivalent to the permeability coefficient of the electrolyte in electrodes. The effective D_{eff} in the LMLE is 3.8×10^{-7} cm^2/s, higher than 1.5×10^{-7} cm^2/s calculated for HMLE (Fig. 2d). The higher D_{eff} in the LMLE indicates a faster wetting process in electrodes, which contributes to a higher D_{Li+} in LMLE compared to that of HMLE. In addition, the electrolyte migration processes in LMLE and HMLE are simulated using Avizo software (see *Note 4 in SI*).[36] As shown in Fig. 2e and video 1, the streamlines passing through LMLE have a more uniform color distribution, indicating homogenous absolute flow velocity of electrolyte. In comparison, HMLE exhibits fewer effective flow lines and inhomogeneous absolute flow velocity along the thickness direction, indicating fewer effective migration paths for the electrolyte to replenish, and potential sluggish diffusion and uneven electrolyte distribution within HMLE [37,38].

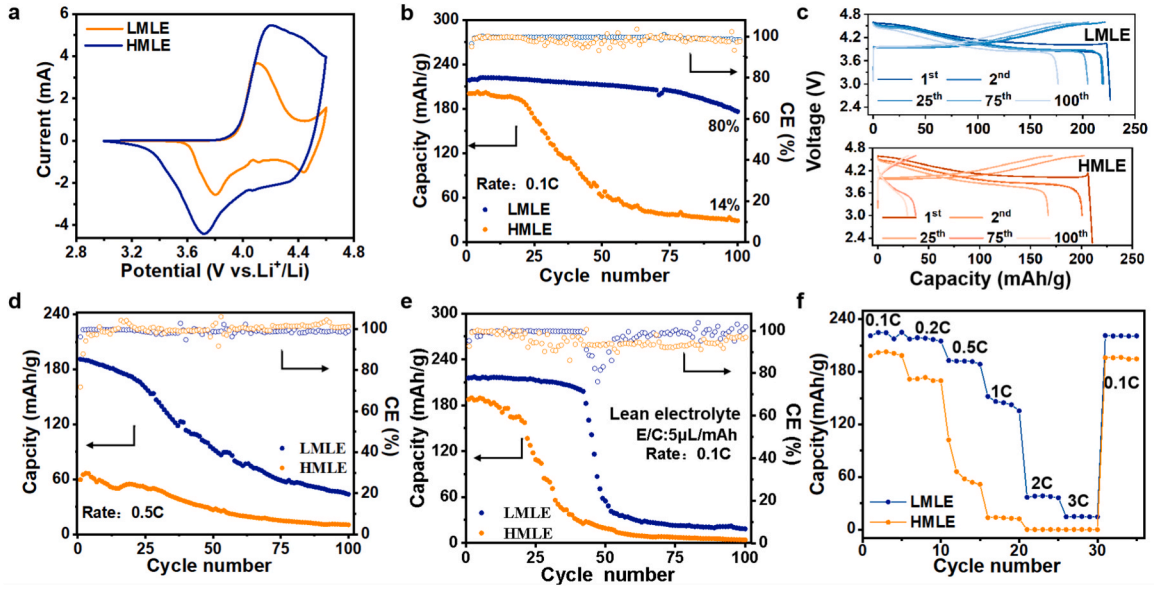

Fig. 3. Electrochemical performances of Li|$LiCoO_2$ cells. (a) CV curves of the LMLE and HMLE at a scan rate of 0.1 mV/s. (b) Cycling performance of cells at 0.1C with flooded electrolyte and (c) corresponding charge and discharge curves at specific cycles. (d) Cycling performance of cells at a high current rate of 0.5C. (e) Cycling performance of cells at 0.1C with the E/C ratio of 5 μ L/mAh. (f) Rate performances.

The electrochemical performance of Li|LMLE and Li|HMLE cells were investigated. All cells are resting for 24 h to realize a full infiltration state of the electrodes. As shown in Fig. 3a, the gap between the oxidation and reduction peaks in cyclic voltammetry (CV) results of HMLE (0.48 V to 0.31 V) is larger and less symmetrical compared to LMLE, indicating higher polarization and weaker electrochemical reversibility. This supports the hypothesis that the uneven pore structure in HMLE hinders mass transport within the battery, resulting in significant polarization and rapid capacity decay. The cycling performance of Li|LMLE and Li|HMLE cells with flooded electrolyte to achieve a fully wetted state was compared. As shown in Fig. 3b-c, during the first cycle, the Li|LMLE cell delivers a specific capacity of 218.6 mAh/g (areal capacity is ~ 4.4 mAh/cm^2) at a current density of 0.1C (1C = 274 mA/g), which is close to the theoretical capacity of LCO at 4.6 V (220 mAh/g), while the Li|HMLE cell reaches only ~ 200 mAh/g (areal capacity is ~ 9.5 mAh/cm^2). The Li|LMLE cell demonstrates stable cycling behavior, retaining 80 % of its capacity after 100 cycles. In contrast, the capacity of the Li|HMLE cell declines rapidly between 20th and 50th cycles, resulting in poor retention of just 14 % after 100 cycles. This can be attributed to the uneven pore structure in HMLE, which restricts ion diffusion, hindering the full participation of the active material in electrochemical reactions and resulting in a lower specific capacity. Cross-sectional analysis after 100 cycles (Fig. S4) shows that the thickness of LMLE increases to 79.9 μm, corresponding to a maximum expansion rate of 17.5 %, whereas HMLE expands to 200 μm with an expansion rate of only 5 %. These findings highlight the lower utilization rate of active material in HMLE, as reflected in its reduced capacity and more pronounced capacity degradation during cycling. For the charge and discharge tests, a different industrial battery operating scenario was simulated with a high current density of 0.5C (Fig. 3d). In these measurements, the first three cycles were conducted at 0.1C for activation but were excluded from the plotted data. The LMLE battery demonstrated excellent performance, maintaining a capacity of 191 mAh/g and a specific capacity of 43 mAh/g after 100 cycles. In contrast, the HMLE battery exhibited an initial specific capacity of only 74 mAh/g, which rapidly declined under the high current density. This stark difference highlights that, at high current densities, the rapid charge and discharge processes necessitate efficient mass transfer of lithium ions during lithiation and delithiation. The ion transport in HMLE, due to its complex pore structure, is sluggish and cannot be replenished during high-rate cycling, leading to significant performance degradation compared to LMLE.

Under near-practical conditions, the electrolyte-to-cathode capacity ratio (E/C) was controlled at 5 μL/mAh with a current density of 0.1C (Fig. 3e). At this low E/C ratio, the initial specific capacity of HMLE decreased significantly compared to measurements with a higher initial electrolyte volume of approximately 150 μL, whereas the capacity of LMLE remained essentially unchanged. This discrepancy is likely due to incomplete electrolyte infiltration in HMLE prior to cycling. HMLE exhibited similar capacity attenuation trends under excess electrolyte conditions (Fig. 3b) and thin electrolyte conditions (Fig. 3e), indicating poor electrolyte penetration during cycling. This observation is consistent with our discussion in Figs. 1 and 2 about the effect of porosity and curvature on electrolyte permeability. In contrast, LMLE maintained stable capacity under excess electrolyte conditions but experienced rapid capacity decay under thin electrolyte conditions, showing an attenuation trend similar to that of HMLE. Even with a larger injection volume (150 μL), the high curvature and low porosity structure of HMLE create local electrolyte deficiencies, exacerbating the “quick fall” in capacity.

The rate performance of LMLE and HMLE batteries, tested at increasing rates from 0.1C to 3C, is shown in Fig. 3f. Li|LMLE cells deliver discharge capacities of 221, 217.5, 193, 152, 37, and 15 mAh/g at rates of 0.1, 0.2, 0.5, 1, 2, and 3C, respectively. Li|HMLE cells, in comparison, provide corresponding capacities of 198, 172, 102, 14, 0.02, and 0.02 mAh/g. When the rate was reduced back to 0.1C, the capacities recovered to 221 mAh/g for LMLE and 196 mAh/g for HMLE. The capacity of HMLE can be restored to 196 mAh/g because its high tortuosity and low porosity hinder effective electrolyte infiltration. As a result, most active materials remain unreacted at high current densities (≥0.5C). However, since the structure remains intact, the capacity recovers when the rate returns to 0.1C. These results indicate that the smaller porosity and higher tortuosity in HMLE significantly limit its rate performance, as its spatial structure cannot efficiently replenish the required amount of Li ions during high-rate cycles, resulting in a considerable reduction in ion transport capacity. In addition, electrochemical impedance spectroscopy (EIS) was performed on lithium metal half-cells constructed with LCO cathodes. The Nyquist plots exhibit semicircles in the high-medium frequency region, corresponding to charge transfer resistance (R_{ct}, Fig. S5). After one cycle, the R_{ct} of the Li|LMLE is 95.9 Ω, lower than that of the HMLE battery (122.3 Ω). After 100 cycles, the R_{ct} increases to 128.1 Ω for LMLE but remained lower than HMLE’s 149.7 Ω. Additional EIS tests on pristine batteries without sufficient standing time prior to testing (Fig. S6) revealed resistances of 390.9 Ω for LMLE and 630.9 Ω for HMLE. These findings corroborate earlier observations: LMLE exhibits faster ion diffusion, effectively penetrating the separator and electrode to establish efficient ion transport paths quickly. In contrast, the complex and uneven pore structure of HMLE lead to poor electrolyte infiltration, higher impedance, and limited ion transport capability, both before and after cycling.

Based on the aforementioned studies, it is hypothesized that the majority of active particles near the current collector are less likely to fully participate in the electrochemical reaction due to weak dynamic properties during the long-term cycling of HMLEs. To validate this hypothesis, structural characterization was performed on electrodes after 100 cycles at lithiated states.

To investigate the impact of electrode thickness on redox heterogeneity, LCO particles near the current collector from both LMLE and HMLEs were extracted using focused ion beam-SEM (Fig. S7) followed by spectro-tomographic scans over the absorption K-edge of the Co element, namely TXM-XANES. This technique enables nanoscale, three-dimensional spatial resolution of the local valence state of the Co element. As shown in Fig. 4a-c, the particle from the HMLE exhibits significantly higher valence inhomogeneity of Co element. Clearly, local area with high Co valence exists at the edge of the particle from HML electrode, which is further confirmed by the XANES plots in Fig. 4d obtained over the area in Fig. S8 [39]. Since the electrodes were cycled 100 times and analyzed in their delithiated states, the overall higher Co valence in the HMLE particle indicates reduced redox homogeneity. This finding aligns with the previously discussed uneven and sluggish mass transfer characteristics observed in thick electrodes.

X-ray photoelectron spectroscopy (XPS) was conducted to analyze the valence states of cobalt near the current collector (Fig. 4e) and the separator (Fig. 4f) [40,41]. On the side closer to the collector, the Co^{4+} signals (782.9 eV, 798.1 eV) were more pronounced with larger peak areas, whereas no significant changes were observed on the separator side. Additionally, Time-of-flight secondary ion mass spectrometry (ToF-SIMS) was employed to evaluate the structure and particulate matter distribution near the current collector (Fig. 4g-h), with the pristine LCO electrode serving as a reference (Fig. S9). The three-dimensional spatial distribution images of LMLE exhibited fewer occupied sites, indicating a lower lithium concentration. In contrast, the HMLE showed a nonuniform yet significantly more occupied distribution, suggesting a higher lithium concentration. This can be attributed to the high tortuosity and low porosity of HMLE, which hinder effective electrolyte infiltration during replenishment. As a result, the reaction depth is shallow, leading to a lower degree of lithiation. The cobalt elements in both electrodes appeared fibrous and densely packed. Integrating the XPS and ToF-SIMS results, it can be inferred that as the electrochemical reaction progresses, the degree of delithiation of active materials near the collector side of the HMLE battery decreases. A substantial portion of these materials fails to participate in the

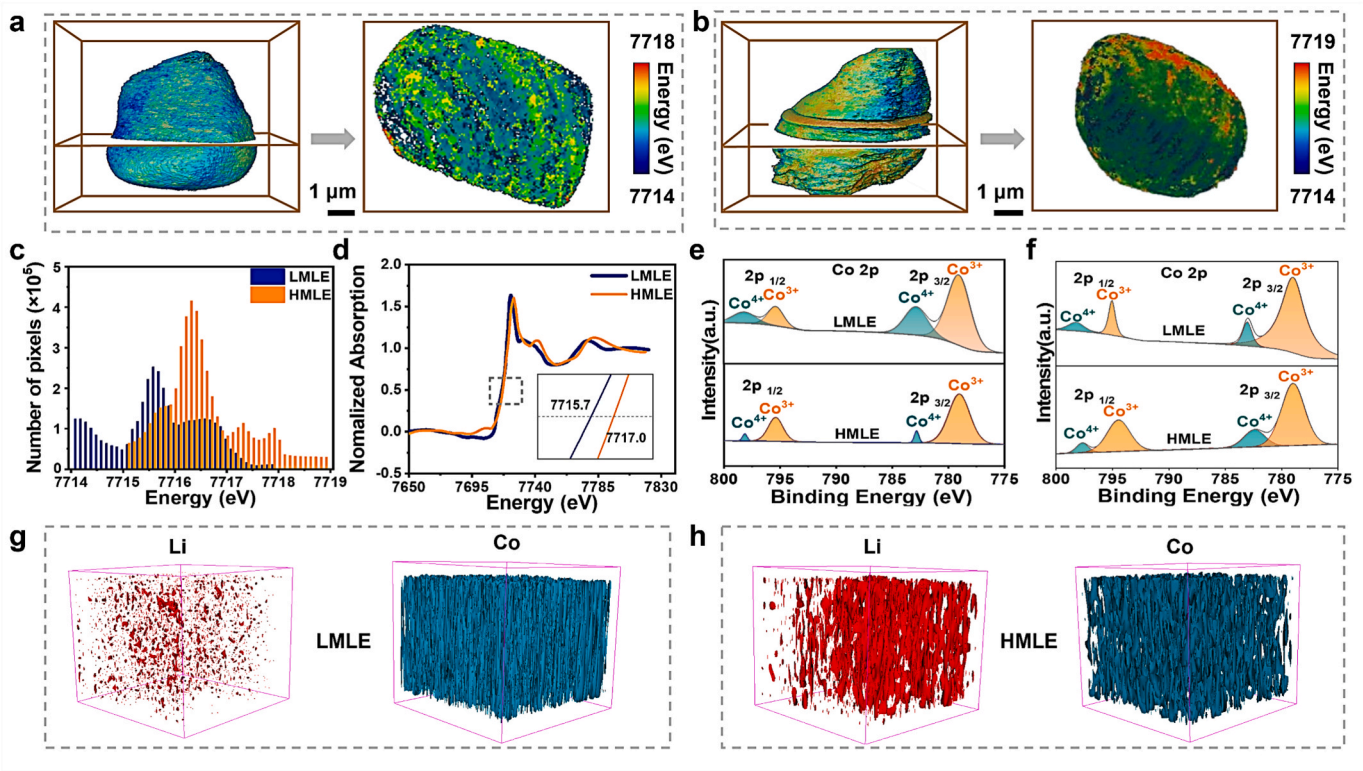

Fig. 4. The nano-scale spectro-microscopic investigation of LMLE and HMLE. (a-b) 3D and 2D energy distribution map obtained by TXM-XANES of (a) LMLE and (b) HMLE. (c) The probability distributions of the edge energy over the K-edges of Co across the whole particle. (d) XANES spectra of and enlarged view. (e-f) The Co 2p XPS spectra of LMLE and HMLE collected at side (e) near the collector and (f) near the separator. (g-h) The distribution and content of Li and Co of (g) LMLE and (h) HMLE harvested near the collector from 3D ToF-SIMS.

electrochemical reaction, leading to a relatively shallow reaction depth. These findings confirm that the slow electrolyte diffusion caused by the uneven pore distribution is the primary reason for the rapid capacity degradation observed in thick HMLE.

Finally, the key findings are summarized in the schematic diagram shown in Fig. 5. Increasing electrode mass loading inevitably alters the electrode structure, resulting in significantly greater thickness, reduced porosity, and increased tortuosity. These structural changes directly

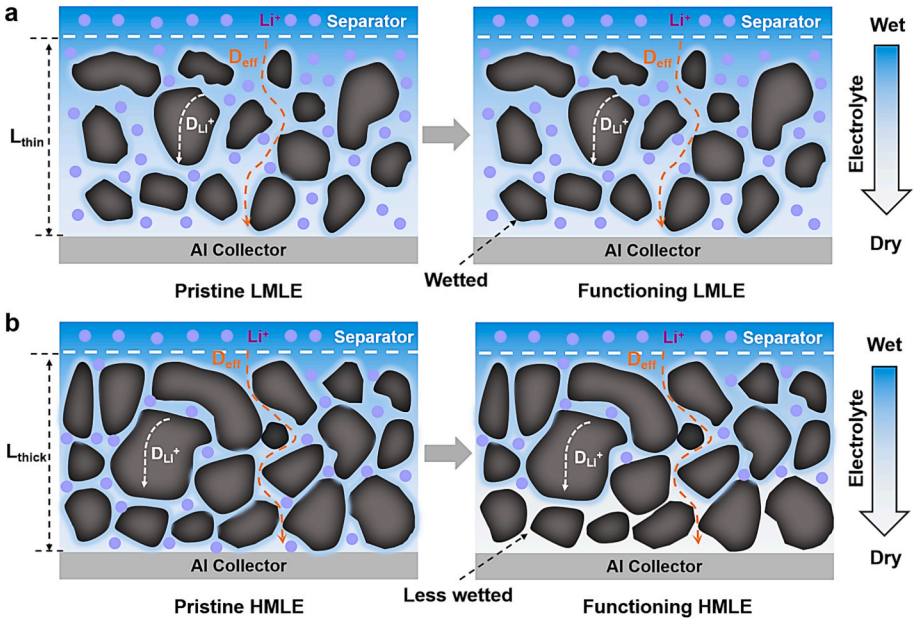

Fig. 5. Schematic illustrating the comparison of mass transfer in LMLE and HMLE. (a) The LMLE features a well-distributed pore structure, enabling active material particles deep within the electrode to participate effectively in charge/discharge cycles while maintaining good electrolyte wettability. (b) In contrast, the HMLE exhibits uneven pore distribution and increased tortuosity, which hinders the electrolyte infiltration and limits the participation of active particles in electrochemical redox.

affect mass transport dynamics within the electrode, including intrinsic ion diffusion (D_{Li}^{+}) within particles and effective electrolyte diffusion (D_{eff}). For both LMLE and HMLE prior to cycling, sufficient electrolyte availability and adequate resting time initially facilitate proper electrode infiltration. However, in thick electrodes (L_{thick}), uneven pore distribution and reduced porosity are more pronounced compared to thin electrodes (L_{thin}). These structural deficiencies increase tortuosity and impede electrolyte infiltration, particularly for particles near the current collector. When electrolyte infiltration becomes insufficient and Li ions cannot replenished, LCO particles tend to partially participate in electrochemical reactions, reducing the overall mean diffusion coefficient. This limitation becomes even more pronounced under high-rate cycling or lean electrolyte conditions. Consequently, poor electrolyte wettability significantly accelerates the degradation of cell performance.

3. Conclusion

Multi-scale imaging techniques including synchrotron micro-CT, nano-scale TXM-XANES, and ToF-SIMS, were employed to investigate the pore microstructure, mass dynamic transfer in thick $LiCoO_2$ electrodes as well as their impacts on electrochemical performance. We demonstrate that poor electrolyte infiltration in thick electrodes, driven by decreased porosity and increased tortuosity, is a key factor in the rapid capacity degradation of cells. In the studied systems, increasing the mass loading of $LiCoO_2$ electrodes from ~ 20 mg/cm^2 to ~ 50 mg/cm^2 raises the electrode thickness from ~ 68 μm to ~ 190 μm, leading to a decline in capacity retention rate from 80 % to 14 %. These adverse effects are particularly pronounced under fast-charge conditions or in lean-electrolyte battery systems. For example, the capacity retention of 68 μm electrodes decreases from 80 % to 23 % when decreasing the electrolyte to 5 μL/mAh. These results demonstrate that optimizing pore distribution, porosity, and tortuosity in thick electrodes to enhance electrolyte infiltration is essential for improving the performance of high-energy–density Li-ion batteries.

CRediT authorship contribution statement

Bowei Li: Writing – review & editing, Writing – original draft, Visualization, Investigation, Formal analysis, Data curation. **Shanfeng Wang:** Writing – review & editing, Writing – original draft, Methodology, Funding acquisition, Formal analysis, Data curation, Conceptualization. **Pan He:** Writing – review & editing, Writing – original draft, Visualization, Supervision, Funding acquisition, Formal analysis. **Zhenyao Huang:** Writing – original draft, Formal analysis. **Bo Mai:** Writing – review & editing, Formal analysis. **Xia Zhang:** Writing – review & editing, Visualization. **Yuhang Chen:** Writing – review & editing, Methodology. **Yuehua Wen:** Writing – review & editing, Formal analysis. **Xiaqing Ran:** Writing – review & editing, Data curation. **Chunhua Han:** Writing – review & editing, Supervision, Conceptualization. **Ingo Manke:** Writing – review & editing. **Kang Dong:** Writing – review & editing, Supervision, Resources, Funding acquisition, Formal analysis, Data curation, Conceptualization. **Mengyu Yan:** Writing – review & editing, Supervision, Methodology, Funding acquisition, Formal analysis, Data curation, Conceptualization.

Declaration of competing interest

The authors declare that they have no known competing financial interests or personal relationships that could have appeared to influence the work reported in this paper.

Acknowledgments

B. L., S. W., and P. H. contributed equally to this work. This work was supported by the National Natural Science Foundation of China (52472244, 52172233, 12405373), the Scientific and Technological Innovation project of the Institute of High Energy Physics, Chinese Academy of Sciences (No. E4545CU2, E35451U2) the Key Research and Development Program of Hubei Province (2022BAA027). P.H. acknowledges the support from the UCL's Global Engagement Funds (GEF-2023/24). We thank Shanghai synchrotron radiation facility for the beamtime allocation at the BL18B beamline for TXM-XANES measurements. B.L. and K.D. acknowledges BESSY II for the beamtime allocation at the BAMline end-station. The authors thank Yongkun Yu for the XPS test and Jiajun Chen for the ToF-SIMS test.

Author contributions

B.L., S.W., and P.H. contributed equally to this work. X.Z. B.L. performed the experiments. S.W. analyzed the TXM-XANES data. Y.W., K. D., Z.H., and B.M. contributed to the initial idea. X.Z. and I.M. conduct μCT measurements. X.R., Y.C., C.H., and K.D. reviewed the manuscript. B.L. and P.H. analyzed all the data and wrote the manuscript. P.H., K.D., and M.Y. edited the manuscript. All authors commented on the manuscript.

Appendix A. Supplementary data

Supplementary data to this article can be found online at https://doi.org/10.1016/j.cej.2025.161931.

Data availability

Data will be made available on request.

References

[1] J. Xu, X. Cai, S. Cai, Y. Shao, C. Hu, S. Lu, S. Ding, High-energy lithium-ion batteries: recent progress and a promising future in applications, *Energy Environ. Mater.* 6 (2023) E12450.
[2] H. Li, Practical evaluation of Li-ion batteries, Joule 3 (2019) 911.
[3] Y. Zhang, W. Hua, Z. Li, X. Ge, K. Huang, J. Huang, H. Ling, L. Zhen, Y. Huang, Multiscale construction of bifunctional electrocatalysts for long-lifespan rechargeable zinc–air batteries, *Adv. Energy Mater.* 2403804 (2024).
[4] T. Yang, K. Zhang, Y. Zuo, J. Song, Y. Yang, C. Gao, T. Chen, H. Wang, W. Xiao, Z. Jiang, D. Xia, Ultrahigh-nickel layered cathode with cycling stability for sustainable lithium-ion Batteries, *Nat. Sustain.* 7 (2024) 1204.
[5] L. Qian, T. Or, Y. Zheng, M. Li, D. Karim, A. Cui, M. Ahmed, H.W. Park, Z. Zhang, Y. Yu, A. Deng, Z. Chen, K. Amine, Critical operation strategies toward high-performance lithium metal batteries, *Renewables* 1 (2023) 114–141.
[6] J. Wang, X. Lei, S. Guo, L. Gu, X. Wang, A. Yu, D. Su, Doping strategy in nickel-rich layered oxide cathode for lithium-ion battery, *Renewables* 1 (2023) 316–340.
[7] J. Lee, Q. Zhang, J. Kim, N. Dupre, M. Avdeev, M. Jeong, W.S. Yoon, L. Gu, B. Kang, Controlled atomic solubility in Mn-rich composite material to achieve superior electrochemical performance for Li-ion batteries, *Adv. Energy Mater.* 10 (2019) 1902231.
[8] J. Wu, Z. Ju, X. Zhang, C. Quilty, K.J. Takeuchi, D.C. Bock, A.C. Marschilok, E. S. Takeuchi, G. Yu, Ultrahigh-capacity and scalable architected battery electrodes via tortuosity modulation, *ACS Nano* 15 (2021) 19109.
[9] X. Yang, T. Liu, C. Wang, Thermally modulated lithium iron phosphate batteries for mass-market electric vehicles, *Nat. Energy* 6 (2021) 176.
[10] J. Wu, X. Zhang, Z. Ju, L. Wang, Z. Hui, K. Mayilvahanan, K.J. Takeuchi, A. C. Marschilok, A.C. West, E.S. Takeuchi, G. Yu, From fundamental understanding to engineering design of high-performance thick electrodes for scalable energy-storage systems, *Adv. Mater.* 33 (2021) 2101275.
[11] R.C. Chiu, T.J. Garino, M.J. Cima, Drying of granular ceramic films: I, effect of processing variables on cracking behavior, *J. Am. Ceram. Soc.***1** 76 (1993) 2257.
[12] K.B. Singh, M.S. Tirumkudulu, Cracking in drying colloidal films, *Phys. Rev. Lett.* 98 (2007) 218302.
[13] M. Ebner, D.W. Chung, R.E. García, V. Wood, Tortuosity anisotropy in lithium-ion battery electrodes, *Adv. Energy Mater.* 4 (2013) 1301278.
[14] D. Tyler, K.S. Puneet, S. Alex, W.F. Gerald, J. Jacob, Measurement of tortuosity and porosity of porous battery electrodes, *J. Electrochem. Soc.* 161 (2014) A599.
[15] Q. Liu, H. An, X. Wang, F. Kong, Y. Sun, Y. Gong, S. Lou, Y. Shi, N. Sun, B. Deng, J. Wang, J. Wang, Effective transport network driven by tortuosity gradient enables high-electrochem-active solid-state batteries, *Natl. Sci. Rev.* 10 (2023) 739.
[16] X. Liu, Y. Zeng, W. Yuan, G. Zhang, H. Zheng, Z. Chen, Advances in multi-scale design and fabrication processes for thick electrodes in lithium-ion batteries, *Energy Rev.* 3 (2024) 100066.
[17] K.G. Gallagher, S.E. Trask, C. Bauer, T. Woehrle, S.F. Lux, M. Tschech, P. Lamp, B. J. Polzin, S. Ha, B. Long, Q. Wu, W. Lu, D.W. Dees, A.N. Jansen, Optimizing areal capacities through understanding the limitations of lithium-ion electrodes, *J. Electrochem. Soc.* 163 (2015) A138.

[18] W.A. Appiah, J. Park, S. Song, S. Byun, M.H. Ryou, Y.M. Lee, Design optimization of LiNi0.6Co0.2Mn0.2O$_2$/graphite lithium-ion cells based on simulation and experimental data, *J. Power Sources* 319 (2016) 147.
[19] A.M. Boyce, X. Lu, D.J.L. Brett, P.R. Shearing, Exploring the influence of porosity and thickness on lithium-ion battery electrodes using an image-based model, *J. Power Sources* 542 (2022) 231799.
[20] K. Fu, X. Li, K. Sun, Z. Zhang, H. Yang, L. Gong, G. Qin, D. Hu, T. Li, P. Tan, Rational design of thick electrodes in lithium-ion batteries by re-understanding the relationship between thermodynamics and kinetics, *Adv. Funct. Mater.* 2409623 (2024).
[21] S. Zhao, B. Wang, Z. Zhang, X. Zhang, S. He, H. Yu, First-principles computational insights into lithium battery cathode materials, *Electrochem. Energy Rev.* 5 (2021) 1.
[22] S. Maiti, M.T. Curnan, K. Maiti, S. Choung, J.W. Han, Accelerating Li-based battery design by computationally engineering materials, *Chem* 9 (2023) 3415.
[23] M. Chouchane, W. Yao, A. Cronk, M. Zhang, Y.S. Meng, Improved rate capability for dry thick electrodes through finite elements method and machine learning coupling, *ACS Energy Lett.* 9 (2024) 1480.
[24] R. Xiong, M. Zhou, L. Li, J. Xu, M. Li, B. Yan, D. Li, Y. Zhang, H. Zhou, Decoupled measurement and modeling of interface reaction kinetics of ion-intercalation battery electrodes, *Energy Storage Mater.* 54 (2023) 836.
[25] E.G. Sukenik, L. Kasaei, G.G. Amatucci, Impact of gradient porosity in ultrathick electrodes for lithium batteries, *J. Power Sources* 579 (2023) 233327.
[26] T. Lyu, F. Luo, D. Wang, L. Bu, L. Tao, Z. Zheng, Carbon/lithium composite anode for advanced lithium metal batteries: design, progress, in situ characterization, and perspectives, *Adv. Energy Mater.* 12 (2022) 2201493.
[27] J. Lu, T. Wu, K. Amine, State-of-the-art characterization techniques for advanced lithium-ion batteries, *Nat. Energy.* 2 (2017) 17011.
[28] S. Peth, R. Horn, F. Beckmann, T. Donath, J. Fischer, A.J.M. Smucker, Three-dimensional quantification of intra-aggregate pore-space features using synchrotron-radiation-based microtomography, *Soil Sci. Soc. Am. J.* 72 (4) (2008) 897–907.
[29] W. Wang, A.N. Kravchenko, A.J.M. Smucker, W. Liang, M.L. Rivers, Intra-aggregate pore characteristics: X-ray computed microtomography analysis, *Soil Sci. Soc. Am. J.* 124 (2012) 17.
[30] D. Zhao, M. Xu, G. Liu, R. Zhang, D. Tuo, Characterization of soil aggregate microstructure under different revegetation types using micro-computed tomography, *Trans. Chin. Soc. Agric. Eng.* 32 (2016) 123.
[31] L. De Chiffre, S. Carmignato, J.P. Kruth, R. Schmitt, A. Weckenmann, Industrial applications of computed tomography, *CIRP Ann.* 63 (2014) 655.
[32] Y. Liu, J.C. Andrews, F. Meirer, A. Mehta, S.C. Gil, P. Sciau, Z. Mester, P. Pianetta, Applications of hard x-ray full-field transmission X-ray microscopy at SSRL, *AIP Conference Proceedings* 1365 (2011) 357.
[33] Q. Yuan, K. Zhang, Y. Hong, W. Huang, K. Gao, Z. Wang, P. Zhu, J. Gelb, A. Tkachuk, B. Hornberger, M. Feser, W. Yun, Z. Wu, A 30 nm-resolution hard X-ray microscope with X-ray fluorescence mapping capability at BSRF, *J. Synchrotron Radiat.* 19 (2012) 1021.
[34] W. Wang, A.N. Kravchenko, A.J.M. Smucker, W. Liang, M.L. Rivers, Intra-aggregate pore characteristics: X-ray computed microtomography analysis, *Soil Sci. Soc. Am. J.* 100 (2012) 143107.
[35] A. Vadakkepatt, B. Trembacki, S.R. Mathur, J.Y. Murthy, Bruggeman's exponents for effective thermal conductivity of lithium-ion battery electrodes, *J. Electrochem. Soc* 163 (2) (2015) A119.
[36] M. Ebner, D.W. Chung, R.E. García, V. Wood, Tortuosity anisotropy in lithium-ion battery electrodes, *Adv. Energy Mater.* 249 (1) (2013) 349.
[37] L. Johannes, H. Johannes, E.A. Andreas, W. Wolfgang, A.G. Hubert, Tortuosity determination of battery electrodes and separators by impedance spectroscopy, *J. Electrochem. Soc.* 163 (7) (2016) A1373.
[38] Zockler, M., Stalling, D., Hege, H. C. Interactive Visualization of 3D-Vector Fields Using Illuminated Streamlines. *VISUALIZATION '96 PROC.* 1996,107.
[39] E. Hu, X. Yu, R. Lin, X. Bi, J.S. Bak, K.-W. Nam, H.L. Xin, C. Jaye, D.A. Fischer, K. Amine, X.Q. Yang, Evolution of redox couples in Li- and Mn-rich cathode materials and mitigation of voltage fade by reducing oxygen release, *Nat. Energy* 3 (2018) 690.
[40] J. Zhong, Q. Chen, C. Guo, W. Peng, Y. Li, F. Zhang, X. Fan, Al^{3+} leaching induced Co^{4+} on CoFeAl layered double hydroxide for enhanced oxygen evolution reaction, *Int. J. Hydrogen Energy* 48 (2023) 23530.
[41] R. Zhang, Y. Lu, L. Wei, Z. Fang, C. Lu, Y. Ni, Z. Xu, S. Tao, P. Li, Synthesis and conductivity properties of $Gd_{0.8}Ca_{0.2}BaCo_2O_{5+\delta}$ double perovskite by sol–gel combustion, *J. Mater. Sci.:Mater. Electron.* 26 (2015) 9941.